THE JOURNAL OF PHYSICAL CHEMISTRY B

pubs.acs.org/JPCB Article

Connections between the Speciation and Solubility of Ni(II) and Co(II) in Molten $ZnCl_2$

Simerjeet K. Gill,* Jiahao Huang, Julia Mausz, Ruchi Gakhar, Santanu Roy, Fernando Vila, Mehmet Topsakal, William C. Phillips, Bobby Layne, Shannon Mahurin, Phillip Halstenberg, Sheng Dai, James F. Wishart, Vyacheslav S. Bryantsev, and Anatoly I. Frenkel*

Cite This: J. Phys. Chem. B 2020, 124, 1253−1258 Read Online

ACCESS | Metrics & More | Article Recommendations | Supporting Information

ABSTRACT: Understanding the factors that control solubility and speciation of metal ions in molten salts is key for their successful use in molten salt reactors and electrorefining. Here, we employ X-ray and optical absorption spectroscopies and molecular dynamics simulations to investigate the coordination environment of Ni(II) in molten $ZnCl_2$, where it is poorly soluble, and contrast it with highly soluble Co(II) over a wide temperature range. In solid $NiCl_2$, the Ni ion is octahedrally coordinated, whereas the $ZnCl_2$ host matrix favors tetrahedral coordination. Our experimental and computational results show that the coordination environment of Ni(II) in $ZnCl_2$ is disordered among tetra- and pentacoordinate states. In contrast, the local structure of dissolved Co(II) is tetrahedral and commensurate with the $ZnCl_2$ host's structure. The heterogeneity and concomitant large bond length disorder in the Ni case constitute a plausible explanation for its lower solubility in molten $ZnCl_2$.

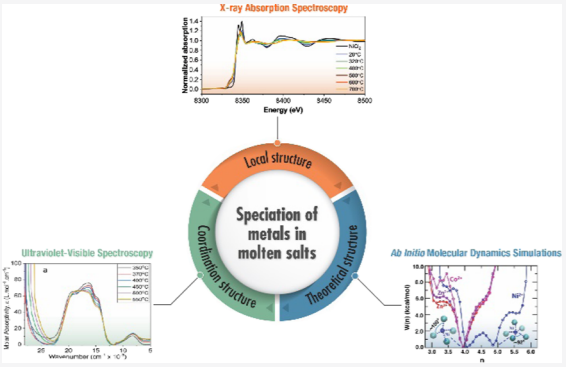

INTRODUCTION

Molten salt reactors (MSRs) are attractive due to their inherently safe design principles, modularity, compatibility with sustainable fuel cycles, and other features that make them leading candidates for future nuclear power installations.[1−3] In MSRs, the fissionable nuclear fuel is dissolved in the molten salt heat transfer fluid, and as the reactor operates, fission products accumulate in the salt while corrosion adds other elements to it as well. Successful MSR deployment and operation depend on managing the solubilities, valence states, and reactivities of the numerous elements within the salt, while maintaining its thermophysical properties as the reactor coolant.[4−6]

Controlling the chemistry of the element soup found in an operating MSR requires an understanding of the structure and properties of the molten salt itself, the thermodynamics and speciation of the elements dissolved in it, and the effects of radiation on their chemistry. For this study, we are interested in the factors that control metal ion solubility in a given molten salt matrix. For a model system, we opted to study the interactions of Ni(II) and Co(II) ions with molten $ZnCl_2$, for multiple reasons. First, the literature[7] reports that Ni(II) is only sparingly soluble in molten $ZnCl_2$, while Co(II) is very soluble, providing two systems whose behavior would be easy to contrast. Second, $ZnCl_2$ is a well-understood, single-component, low-melting-point (290 °C) salt system.[8,9] Third, nickel is a common component of MSR reactor alloys and thus a major anticipated corrosion product, hence it is particularly important to study. Finally, all of the three metal ions in this system (Co, Ni, and Zn) can be investigated by extended X-ray absorption fine structure (EXAFS) and X-ray absorption near-edge structure (XANES).

EXAFS and XANES are element-specific techniques that can probe the range of metal ion speciation (local coordination and structure) present in molten salts under high-temperature conditions relevant to MSRs.[10] EXAFS provides direct information on the first-shell neighbors of metal atoms in terms of coordination number (CN), interatomic distance (R), and their mean-squared disorder (σ^2). It has been used to study the local structure of ionic species for various applications such as catalysis[11,12] and batteries,[13,14] and in molten salts to some extent.[15−18] XANES provides information about electronic states and symmetry in the local environment around the absorbers.

Due to the inherent heterogeneities and enhanced disorder expected in the molten state, a multimodal approach for local structure characterization is required. Multiple species may reveal themselves through the nearest-neighbor coordination,

Received: January 8, 2020
Published: January 24, 2020

https://dx.doi.org/10.1021/acs.jpcb.0c00195
J. Phys. Chem. B 2020, 124, 1253−1258

and for their characterization, EXAFS is an excellent tool. In many cases, the signatures of a unique local environment may come in the form of a three-body correlation, such as off-center displacement of a central atom in an octahedral cage. For that purpose, XANES and optical ultraviolet−visible (UV−vis) spectroscopy are powerful probes.[19−22] In the disordered environments of molten salts, where the pair distributions of atoms can be far from Gaussian, the applicability of standard EXAFS fitting methods becomes limited[23−25] and molecular dynamics (MD) can provide the key to interpretation.[24,26,27] We employed each of these approaches to understand these salt and solute systems.

EXPERIMENTAL AND MODELING DETAILS

XANES and EXAFS data were collected using a custom-designed and -built high-temperature cell on the ISS (8-ID) and QAS (7-BM) beamlines of the National Synchrotron Light Source II (NSLS-II) at Brookhaven National Laboratory and were analyzed by the Demeter package.[28] The concentrations of Ni(II) and Co(II) used were 1 wt %, meaning that Co(II) was fully dissolved at all temperatures, but Ni(II) was only fully dissolved at ∼500 °C and above.[7] Additional details of sample preparation, cell design, and XAFS data processing and analysis are in the Supporting Information (Figures S1−S13). Details of the setup for high-temperature in situ optical absorption measurements of molten salts and sample preparation for UV−vis spectroscopy are given in the Supporting Information (Section 4, Figures S14 and S15). Details on the ab initio MD (AIMD) simulation procedure are given in the Supporting Information (Section 5, Figures S16−S19). Details on the theoretical XANES modeling are given in the Supporting Information (Section 6).

RESULTS

The Ni and Co K-edge XANES spectra over the temperature range of 20−700 °C are shown in Figure 1. The evolution of the Ni XANES spectra with temperature shows spectral changes in two energy regions: (1) the change in the main peak (also known as the white line) shape and (2) an intensity increase in the pre-edge region (Figure 1a,b). Comparison with a solid $NiCl_2$ reference sample shows that Ni(II)−$ZnCl_2$ at room temperature (RT) has the same type of a double-peak structure in the main peak region, indicating that the environment of Ni(II) in solid $ZnCl_2$ at RT is also octahedral (O_h) as in pure $NiCl_2$. The presence of the double-peak structure in the white line region of Ni K-edge in $NiCl_2$ was also observed in theoretical XANES simulations (Figure S20). However, after increasing the temperature to 400 °C, the double-peak structure decreases in intensity and transforms to a single peak at 500 °C, indicating that a structural transformation occurred between 320 and 500 °C. The white line region shows a single peak between 500 and 700 °C. Based on the XANES, Ni K-edge spectra can be divided into three main temperature regions: (1) an insoluble, frozen solution region that persists until ca. 320 °C, (2) the partially soluble region (between 320 and 500 °C), and (3) the fully soluble region (between 500 and 700 °C). In the pre-edge region (around 8330−8340 eV), the bulk $NiCl_2$ spectrum shows weak signal intensity, as expected for the centrosymmetric O_h structure of bulk $NiCl_2$.[29] The Ni(II)−$ZnCl_2$ spectra have much higher intensity in that region at all temperatures, indicating that the environment around Ni(II) is non-centrosymmetric and becomes more distorted at elevated temperatures.

In contrast to Ni, the Co K-edge XANES spectra show much more subtle structural changes in the white line region between 20 and 320 °C, featuring a visible shoulder, whereas between 320 and 700 °C, the single-peak shape is preserved, as indicated by arrows in Figure 1c. The bulk $CoCl_2$ adopts a centrosymmetric (O_h) structure, similar to $NiCl_2$, and its theoretical XANES calculations also feature a split-peak at the white line (Supporting Information, Figure S20). The white line features, indicated by arrows in Figure 1c, show that the structure of the sample at 20 °C differs from pure $CoCl_2$ as well as the molten state. In the pre-edge region (around 7705−7715 eV, Figure 1d), the RT spectrum shows a small increase in intensity, which suggests that the RT structure is different from the standard O_h $CoCl_2$, whereas the spectra from 320 °C onward do not change significantly across the entire temperature range. The Co XANES spectra can thus be divided into two temperature regions: (1) the RT frozen solution region and (2) the fully soluble region from 320 to 700 °C.

Ni K-edge EXAFS data in *k*-space and *r*-space are shown in Figures S12 and 2a, respectively. Co K-edge data are presented in Figures S9 and 2b. Importantly, the Ni EXAFS spectra at 20

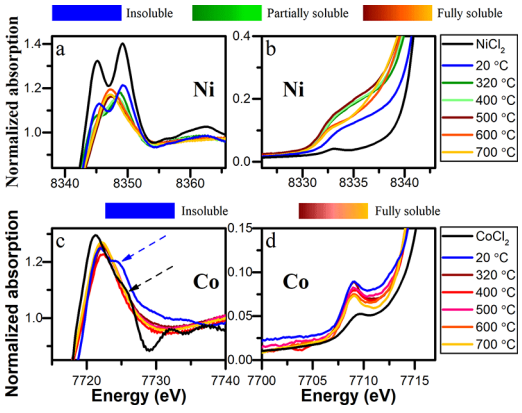

Figure 1. K-edge XANES spectra for (a, b) 1 wt % Ni(II) and (c, d) 1 wt % Co(II) in $ZnCl_2$, showing the white line regions (a, c) and pre-edge regions (b, d). Different temperature regions are colored accordingly.

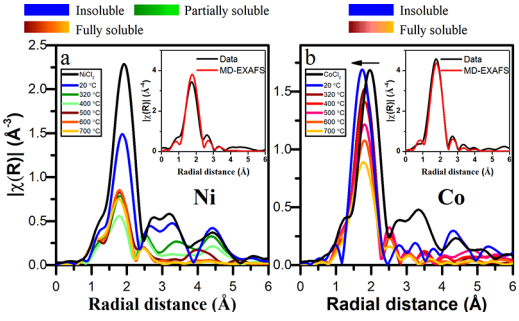

Figure 2. Ni K-edge and Co K-edge Fourier-transformed EXAFS spectra for (a) 1 wt % Ni(II) and (b) 1 wt % Co(II) in $ZnCl_2$ from 20 to 700 °C, with reference $NiCl_2$ and $CoCl_2$, respectively. Different temperature regions are colored accordingly. Insets show qualitative agreement between ab initio MD-simulated EXAFS (500 °C) and experimental EXAFS (600 °C) spectra for Ni and Co absorption edges, respectively.

https://dx.doi.org/10.1021/acs.jpcb.0c00195
J. Phys. Chem. B 2020, 124, 1253−1258

°C resemble pure $NiCl_2$, while at higher temperatures, the higher-order contributions (between 2.5 and 5 Å) change shape and strongly diminish, consistent with the onset of a strongly disordered state (in agreement with the observations made based on XANES data).

In contrast, the Co(II)−Cl peak position in the EXAFS spectrum at 20 °C is shifted compared to pure $CoCl_2$, as shown by the arrow in Figure 2b, which indicates the subtle change in structure for Co(II) in $ZnCl_2$ as compared to $CoCl_2$, in agreement with XANES observations. This shift in the peak toward the lower distances is indicative of Co−Cl interactions occurring at longer distances for $CoCl_2$ compared to Co(II) in $ZnCl_2$ at RT. Compared to the behavior of Co data (Figure 2b), the Ni EXAFS spectra show a dramatic decrease in the first peak intensity, indicating a much stronger structural disorder. The Co data show much more gradual changes in intensity with temperature, consistent with the previous observations made with Co K-edge XANES. In both cases, the changes may be caused by the decrease in Ni(II)(Co(II))−Cl CN, the increase in σ^2, or the combination of these effects. To obtain a detailed picture of structural changes, we performed quantitative analyses of XANES and EXAFS data, as described below. The details of the EXAFS fitting procedure for all samples, the values of fitting parameters (Tables S1 and S2), fit results (Tables S3−S6), and fit figures (Figures S8−S13) are given in the Supporting Information.

We focus the discussion on the behavior of the Co(II)-containing sample first. Figure 3 shows the results of the quantitative analysis. For bulk $CoCl_2$, the results agree qualitatively with the expected Oh structure, in agreement with qualitative XANES results. For RT Co(II) in $ZnCl_2$, we observe the CN of 4. For this structure, there might be two possibilities: (1) a single-phase transition structure that Co(II) adopts before becoming fully soluble and (2) a heterogeneous mixture of the O_h starting structure and the tetrahedral, fully soluble structure (vide infra). It is difficult to distinguish between these possibilities using EXAFS alone as it is an average technique.

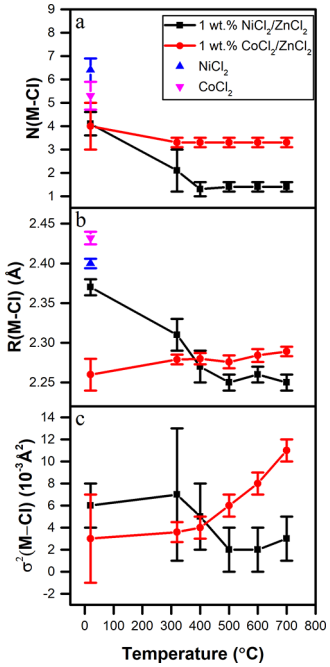

Figure 3. Quantitative EXAFS results: (a) CN, (b) *R*, and (c) σ^2 of the M−Cl bond (M = Co(II), Ni(II)).

The bond length for RT Co(II) in the $ZnCl_2$ structure (2.26 Å) is significantly shorter than that in bulk $CoCl_2$ (2.43 Å). This is consistent with the lower coordination we observe for RT Co(II) in the $ZnCl_2$ structure (CN = 4) as compared to that in bulk $CoCl_2$ structure (5.3 ± 0.6). The data are shown in Figures 1 and 2, and the analysis results (Figure 3) show that the local Co(II) environment does not change significantly over the temperature range studied. The gradual increase of the Co(II)−Cl distance and its disorder with temperature (Figure 3b,c) are expected.[30] The overall trends are consistent with the predominantly single-phase Co(II) dissolved in $ZnCl_2$ because, in the molten state, Zn is also tetrahedrally coordinated.

EXAFS results for the Ni-containing sample at RT show that the CN = 4.1 ± 0.5, whereas for pure $NiCl_2$, the CN = 6.4 ± 0.5, as expected.[29] One possible explanation for the CN of 4 for Ni(II) in $ZnCl_2$ at RT would be that Ni is tetracoordinated (e.g., tetrahedral or square planar) in $ZnCl_2$. This model contradicts both the Ni K-edge XANES behavior in the main peak region (Figure 1a), which shows similar split as the bulk $NiCl_2$ and the Ni K-edge EXAFS behavior in *r*-space (Figure 2a), showing a similar short-range order in both samples. As suggested from these similarities, the local structure of Ni(II) in $ZnCl_2$ at RT should be octahedral, as in bulk $NiCl_2$. A possible reason for the lower (compared to the bulk) CN value of the Ni(II)−$ZnCl_2$ sample at RT is the surface truncation effect, common to metal nanoparticles,[31] whereas Ni(II) cations on the surface of $NiCl_2$ nanocrystallites have fewer Cl neighbors, thereby lowering the ensemble-average Ni(II)−Cl CN. In addition, as evident from the pre-edge behavior of Ni K-edge XANES, the octahedral environment of Ni is more distorted than that in pure $NiCl_2$, causing the increase of the absorption coefficient in the 1s−3d region.[32] Another possible explanation of the apparent reduction of the CN from its expected value of 6 in the octahedral Ni−Cl environment is the correlation between the CN and the Debye−Waller factor value in the fit.

In the molten state, Ni EXAFS results (CN, *R*, and σ^2) show an unexpected trend. The Ni−Cl CN decreases below 2 (Figure 3a), an anomalously low number, in contrast to Co(II)−Cl EXAFS results that remain consistent with the RT value of the CN = 4. In addition, the *R* and σ^2 values for the Ni−Cl bond (Figure 3b,c) decrease abruptly in the partially soluble regime, in contrast to their counterparts in Co(II)−Cl, which show a gradual increase with temperature, as expected. The explanation is likely to be found in the details of the coordination environment of Ni(II).

UV−vis spectroscopy provides a direct probe of the electronic structure and coordination environment of each species (Co or Ni(II)) in the molten state. The optical spectra for Co(II) and Ni(II) in $ZnCl_2$ media are shown in Figure 4a,b, respectively. For both Co(II) and Ni(II), the charge-transfer band located at the high-wavenumber (low-wavelength) region was observed to shift to lower energies with the increasing temperature, as expected, due to the decrease in the energy required to elicit the charge transfer between Cl^- and the relevant cation.[33] Aside from this similarity, the spectra of Co(II) and Ni(II) differ greatly in $ZnCl_2$.

The spectrum of Co(II) in $ZnCl_2$ is composed of three prominent peaks in the visible region. The three peaks in the (14−16) × 10^3 cm^{-1} region have been assigned to transitions

https://dx.doi.org/10.1021/acs.jpcb.0c00195
J. Phys. Chem. B 2020, 124, 1253−1258

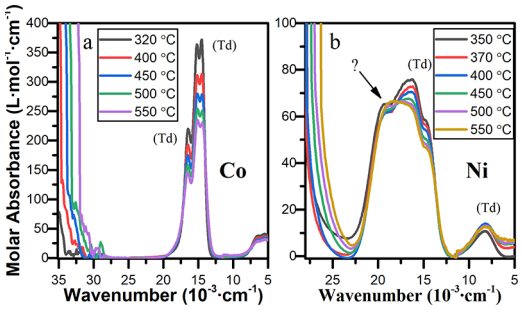

Figure 4. Optical absorption spectra of (a) Co(II) and (b) Ni(II) as a function of temperature.

from the A_2 ground state to the excited T_1 (^4P) states, while a small diffused feature with a maximum around 5.6×10^3 cm^{-1} has been assigned to the A_2 to T_1 (^4F) transition.[34] The spectra show an overall decrease in the peak intensity with temperature. The decrease in peak intensity might be attributed to the increased ionicity of Co−Cl bond, as explained by Gruen et al.[34] Additionally, the increased population of thermally excited states at higher temperatures would result in decreased number of ground state electrons available for electronic absorption, leading to decreased molar absorbance with temperature.

In contrast to the conventional behavior of the Co(II) spectra with temperature, the spectrum of Ni(II) shows significant changes with temperature. The peak around 8×10^3 cm^{-1} has been attributed to a transition from ground state T_1 to excited state $A_2(^3F)$, while the two peaks around 14×10^3 and 15×10^3 cm^{-1} have been attributed to the transitions to excited $T_1(^3P)$ states for Ni(II).[34] Ni(II) ions in molten $ZnCl_2$, in the fully soluble regime, are expected to occupy tetrahedral sites by isomorphously substituting Zn^{2+} ions in the Zn^{2+}−Cl^- network, thus necessitating a structural transformation from the native O_h centrosymmetry of pure $NiCl_2$. We note, however, that Ni(II) does not adopt a symmetric tetrahedral environment, but, instead, stabilizes in a distorted tetrahedral geometry. The descriptor of this distortion is a feature (shown by an arrow in Figure 4b) at 20×10^3 cm^{-1} that cannot be indexed to the tetrahedral[35] symmetry. In summary, the optical absorption results of Ni(II) show the heterogeneous environment of the chlorocomplex formed in the $ZnCl_2$ melt.

DISCUSSION

To reconcile these observations with the underestimated CN of Ni(II)−Cl bonds (vide supra), we briefly revisit the applicability of the EXAFS method to studies of materials with strong bonding disorder, such as molten salts. We propose that, in the case of molten salts, the commonly used approximation of a Gaussian form to the radial distribution function $g(r)$ is wrong,[23] resulting in the underestimated CNs and σ^2 values. To verify this hypothesis and to correct for the artifacts caused by asymmetry of the $g(r)$, ab initio MD (AIMD) simulations were performed for 6 mol % of $NiCl_2$ or $CoCl_2$ solutes in molten $ZnCl_2$ at 500 °C (see Section 5 in the Supporting Information for details). Theoretical EXAFS spectra were calculated for each time step and averaged over all Ni(II) or Co(II) atoms in the simulation box. The insets of Figure 2 show that the MD-EXAFS spectra for 6 mol % Co(II) and Ni(II) absorbers calculated at 500 °C and averaged over 1000 AIMD snapshots are in qualitative agreement with the corresponding experimental spectra at 600 °C. (The difference in the experimental and theoretical concentrations and the resultant difference in temperature effects prevent the accurate quantitative analysis of the MD-EXAFS data; hence, we chose to use the experimental conditions (600 °C) that best match up with the theoretical calculation.) The *k*-space experimental and MD-EXAFS spectra for both Ni and Co K-edges are shown in Figure S19. The MD-EXAFS spectra were scaled by the experimentally obtained values of Ni and Co amplitude reduction factors (0.78 and 0.72, respectively), and the Fourier transforms were performed in the *k*-range from 3 to 8 $Å^{-1}$.

Good qualitative agreement between the theoretical MD-EXAFS data and the experimental spectra provides an opportunity to understand the unusual effects seen in Figure 3. The explanation of the discrepancy between the Ni(II) and Co(II) behavior is due to the bimodal nature of the Ni(II) environment, in agreement with the UV−vis data. Figure 5

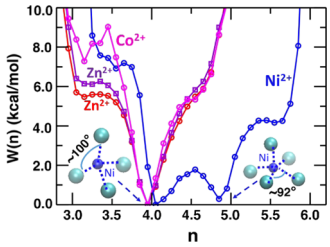

Figure 5. Free-energy profiles in coordination number space, highlighting two different thermodynamically stable coordination states of Ni(II): tetrahedral and square-pyramidal geometries.

identifies the coexistence of predominant four- and five-coordinated Ni(II)−Cl structures that exchange rapidly, as the barrier (~2 kcal/mol) is small and comparable to thermal energy at 500 °C. On the other hand, the Co(II) environment is unimodal (tetrahedral), in agreement with the UV−vis data. From the distribution of the Ni(II)−Cl distances in the four- and five-coordinated states (Figure S18 and Table S7 in the Supporting Information), it is evident that the latter adopts a longer Ni(II)−Cl distance with larger disorder. Furthermore, the computed *k*-space EXAFS spectrum for the five-coordinated state is slightly out of phase than that for the four-coordinated state (Figure S18). Therefore, the ensemble of highly disordered interconverting coordination structures causes a drop in the EXAFS oscillation intensity, as shown in Figure 2.

In addition to explaining the anomalously low apparent CNs in the Ni K-edge EXAFS results, the MD simulations also help with the interpretation of the UV−vis spectra (Figure 4b). MD simulations indicate that the O_h symmetry of Ni(II) is less stable in molten $ZnCl_2$ salts than that in the distorted, pentacoordinated square-pyramidal structure, giving rise to the feature at 20×10^3 cm^{-1}, as shown in Figure 4b.

By combining all the results, we attribute the main difference in the speciation of Ni(II) and Co(II) to the competing forces between ordering and disordering of coordination shells in fully soluble state. The contribution of disorder is stronger for Ni(II) than for Co(II), as predicted from the differences in their electronic configurations. According to the crystal field theory, in the high-spin state, Ni(II) (d^8 configuration) is most strongly stabilized in the octahedral (O_h) environment, while Co(II) (d^7) exhibits a weak Jahn−Teller effect in the O_h field due to unequal occupancy of degenerate nonbonding t_{2g}

https://dx.doi.org/10.1021/acs.jpcb.0c00195
J. Phys. Chem. B 2020, 124, 1253−1258

orbitals. This rationalizes our observation that at RT, Ni(II) in $ZnCl_2$ prefers the O_h environment, but Co(II) in $ZnCl_2$ adopts a more stable tetrahedral (T_d) coordination geometry. The metal CN tends to decrease from RT to temperatures above the melting point, as the packing density decreases and the entropy effects become more important. As shown above, in the molten state, there is no driving force for Co(II) to coexist in multiple environments in the melt because it was already in T_d at low T. The situation is quite different for Ni(II), due to the Jahn–Teller effect in the T_d environment caused by partial occupancy of bonding t_2 orbitals. A coexistence of multiple minima for Ni(II) observed by AIMD simulations (Figure 5) implies competing distortion modes away from a regular tetrahedron. To lift the electronic degeneracy, the four-coordinate Ni(II) undergoes angular distortion from T_d (D_{2d}) symmetry by a vibronic coupling with modes of E symmetry, while the five-coordinate Ni(II) affords a pseudo-square-pyramidal geometry (see Figure S18).

CONCLUSIONS

Based on a combination of X-ray absorption spectroscopy and optical spectroscopy experiments and their interpretation using ab initio molecular dynamics simulations, we obtained, for the first time, strong dynamic heterogeneity in the coordination environments of Ni(II) dissolved in molten $ZnCl_2$, a prototype system for modeling molten salt reactor environment. That heterogeneity was explained in terms of the coexistence of several coordination environments of Ni and the concomitant large bond length disorder, in contrast to the behavior of Co(II) in molten $ZnCl_2$. Our results provide a plausible explanation for lower solubility observed for dissolved Ni(II) with respect to Co(II) in the molten $ZnCl_2$ matrix.

ASSOCIATED CONTENT

Supporting Information

The Supporting Information is available free of charge at https://pubs.acs.org/doi/10.1021/acs.jpcb.0c00195.

Experimental details on materials, sample preparation; X-ray absorption spectroscopy; UV–vis spectroscopy; EXAFS data fitting; ab initio molecular dynamics simulations; theoretical XANES simulations; setup for high temperature in situ optical absorption measurement of molten salts; molten zinc chloride solution containing $NiCl_2$ (purple color) and $CoCl_2$ (bluecolor) in quartz cell (PDF)

AUTHOR INFORMATION

Corresponding Authors

Simerjeet K. Gill – *Nuclear Science and Technology Department, Brookhaven National Laboratory, Upton, New York 11973, United States*; Email: gills@bnl.gov

Anatoly I. Frenkel – *Department of Materials Science and Chemical Engineering, Stony Brook University, Stony Brook, New York 11794, United States; Chemistry Division, Brookhaven National Laboratory, Upton, New York 11973, United States*; orcid.org/0000-0002-5451-1207; Email: frenkel@bnl.gov

Authors

Jiahao Huang – *Department of Materials Science and Chemical Engineering, Stony Brook University, Stony Brook, New York 11794, United States*

Julia Mausz – *Ludwig-Maximilians-Universität München, 80539 München, Germany*

Ruchi Gakhar – *Pyrochemistry and Molten Salt Systems Department, Idaho National Laboratory, Idaho Falls, Idaho 83415, United States*

Santanu Roy – *Chemical Sciences Division, Oak Ridge National Laboratory, Oak Ridge, Tennessee 37831, United States*; orcid.org/0000-0001-6991-8205

Fernando Vila – *Physics Department, University of Washington, Seattle, Washington 98195, United States*; orcid.org/0000-0002-6508-4896

Mehmet Topsakal – *Nuclear Science and Technology Department, Brookhaven National Laboratory, Upton, New York 11973, United States*

William C. Phillips – *Pyrochemistry and Molten Salt Systems Department, Idaho National Laboratory, Idaho Falls, Idaho 83415, United States*

Bobby Layne – *Chemistry Division, Brookhaven National Laboratory, Upton, New York 11973, United States*

Shannon Mahurin – *Chemical Sciences Division, Oak Ridge National Laboratory, Oak Ridge, Tennessee 37831, United States*; orcid.org/0000-0003-3792-1631

Phillip Halstenberg – *Chemical Sciences Division, Oak Ridge National Laboratory, Oak Ridge, Tennessee 37831, United States; Department of Chemistry, University of Tennessee, Knoxville, Tennessee 37996, United States*; orcid.org/0000-0002-6030-4503

Sheng Dai – *Chemical Sciences Division, Oak Ridge National Laboratory, Oak Ridge, Tennessee 37831, United States; Department of Chemistry, University of Tennessee, Knoxville, Tennessee 37996, United States*; orcid.org/0000-0002-8046-3931

James F. Wishart – *Chemistry Division, Brookhaven National Laboratory, Upton, New York 11973, United States*; orcid.org/0000-0002-0488-7636

Vyacheslav S. Bryantsev – *Chemical Sciences Division, Oak Ridge National Laboratory, Oak Ridge, Tennessee 37831, United States*; orcid.org/0000-0002-6501-6594

Complete contact information is available at: https://pubs.acs.org/10.1021/acs.jpcb.0c00195

Notes

The authors declare no competing financial interest.

ACKNOWLEDGMENTS

The authors would like to thank Dr. Klaus Attenkofer for useful discussions on experimental design and help with XAS data collection and Dr. Eli Stavitski for help with XAS data collection. This work was supported as part of the Molten Salts in Extreme Environments Energy Frontier Research Center, funded by the U.S. Department of Energy, Office of Science. BNL, INL, and ORNL are operated under DOE contracts DE-SC0012704, DE-AC07-05ID14517, and DE-AC05-00OR22725, respectively. This research used resources of the ISS (8-ID) and QAS (7-BM) beamlines at the National Synchrotron Light Source II operated by the Brookhaven National Laboratory under Contract No. DE-SC0012704, a U.S. Department of Energy (DOE), Office of Science User Facility. This research used resources of the Oak Ridge Leadership Computing Facility at the Oak Ridge National Laboratory, supported by the Office of Science of the U.S. Department of Energy under contract No. DE-AC05-

00OR22725. This work used resources supported, in part, by the U.S. Department of Energy, Office of Science, Basic Energy Sciences, Materials Science and Engineering Division, Theoretical Condensed Matter Physics Program contract No. DE-FG02-97ER45623, with computational support from the National Energy Research Scientific Computing Center (NERSC), a U.S. Department of Energy, Office of Science User Facility operated under Contract No. DE-AC02-05CH11231.

REFERENCES

(1) LeBlanc, D. Molten salt reactors: A New Beginning for an Old idea. *Nucl. Eng. Des.* **2010**, *240*, 1644−1656.
(2) Serp, J.; Allibert, M.; Beneš, O.; Delpech, S.; Feynberg, O.; Ghetta, V.; Heuer, D.; Holcomb, D.; Ignatiev, V.; Kloosterman, J. L.; Luzzi, L.; Merle-Lucotte, E.; Uhlíř, J.; Yoshioka, R.; Zhimin, D. The Molten Salt Reactor (MSR) in Generation IV: Overview and Perspectives. *Prog. Nucl. Energy* **2014**, *77*, 308−319.
(3) Elsheikh, B. M. Safety Assessment of Molten Salt Reactors in Comparison with Light Water Reactors. *J. Radiat. Res. Appl. Sci.* **2013**, *6*, 63−70.
(4) Williams, D. F. *Assessment of Candidate Molten Salt Coolants for the NGNP/NHI Heat-Transfer Loop*, United States, 2006.
(5) Serrano-López, R.; Fradera, J.; Cuesta-López, S. Molten Salts Database for Energy Applications. *Chem. Eng. Process.* **2013**, *73*, 87−102.
(6) Sohal, M. S.; Ebner, M. A.; Sabharwall, P.; Sharpe, P. *Engineering Database of Liquid Salt Thermophysical and Thermochemical Properties*; Idaho National Laboratory (INL), 2010.
(7) Kerridge, D. H.; Sturton, I. Fused Zinc Chloride, Part II: Some Solubility Measurements. *Inorg. Chim. Acta* **1974**, *8*, 27−30.
(8) Biggin, S.; Enderby, J. The Structure of Molten Zinc Chloride. *J. Phys. C: Solid State Phys.* **1981**, *14*, 3129.
(9) Price, D. L.; Saboungi, M. L.; Susman, S.; Volin, K. J.; Wright, A. C. Neutron Scattering Function of Vitreous and Molten Zinc Chloride. *J. Phys.: Condens. Matter* **1991**, *3*, 9835−9842.
(10) Hardacre, C. Application of EXAFS to Molten Salts and Ionic Liquid Technology. *Annu. Rev. Mater. Res.* **2005**, *35*, 29−49.
(11) Tibiletti, D.; Fonseca, A. A.; Burch, R.; Chen, Y.; Fisher, J. M.; Goguet, A.; Hardacre, C.; Hu, P.; Thompsett, D. DFT and In Situ EXAFS Investigation of Gold/Ceria−Zirconia Low-Temperature Water Gas Shift Catalysts: Identification of the Nature of the Active Form of Gold. *J. Phys. Chem. B* **2005**, *109*, 22553−22559.
(12) Sinfelt, J. H.; Via, G. H.; Lytle, F. W. Application of EXAFS in Catalysis. Structure of Bimetallic Cluster Catalysts. *Catal. Rev.* **1984**, *26*, 81−140.
(13) Giorgetti, M. A Review on the Structural Studies of Batteries and Host Materials by X-Ray Absorption Spectroscopy. *ISRN Mater. Sci.* **2013**, *2013*, 1−22.
(14) Lin, F.; Liu, Y.; Yu, X.; Cheng, L.; Singer, A.; Shpyrko, O. G.; Xin, H. L.; Tamura, N.; Tian, C.; Weng, T.-C.; Yang, X.-Q.; Meng, Y. S.; Nordlund, D.; Yang, W.; Doeff, M. M. Synchrotron X-ray Analytical Techniques for Studying Materials Electrochemistry in Rechargeable Batteries. *Chem. Rev.* **2017**, *117*, 13123−13186.
(15) Okamoto, Y.; Akabori, M.; Motohashi, H.; Itoh, A.; Ogawa, T. High-Temperature XAFS Measurement of Molten Salt Systems. *Nucl. Instrum. Methods Phys. Res., Sect. A* **2002**, *487*, 605−611.
(16) Sun, J.; Guo, X.; Zhou, J.; Dai, J.; Song, S.; Bao, H.; Lin, J.; Yu, H.; He, S.; Jiang, F.; Long, D.; Zhang, L.; Wang, J.-Q. Investigation of the Local Structure of Molten ThF4-LiF and ThF4-LiF-BeF2 Mixtures by High-Temperature X-ray Absorption Spectroscopy and Molecular-Dynamics Simulation. *J. Synchrotron Radiat.* **2019**, *26*, 1733−1741.
(17) Smith, A. L.; Verleg, M. N.; Vlieland, J.; de Haas, D.; Ocadiz-Flores, J. A.; Martin, P.; Rothe, J.; Dardenne, K.; Salanne, M.; Gheribi, A. E.; Capelli, E.; van Eijck, L.; Konings, R. J. M.; et al. In Situ High-Temperature EXAFS Measurements on Radioactive and Air-Sensitive Molten Salt Materials. *J. Synchrotron Radiat.* **2019**, *26*, 124−136.
(18) Bessada, C.; Rollet, A.-L. In Situ Spectroscopy in Molten Fluoride Salts. In *Molten Salts Chemistry*; Elsevier, 2013; pp 33−47.
(19) Farges, F.; Brown, G. E.; Rehr, J. J. Ti K-edge XANES Studies of Ti Coordination and Disorder in Oxide Compounds: Comparison Between Theory and Experiment. *Phys. Rev. B* **1997**, *56*, 1809−1819.
(20) Frenkel, A. I.; Feldman, Y.; Lyahovitskaya, V.; Wachtel, E.; Lubomirsky, I. Microscopic Origin of Polarity in Quasiamorphous $BaTiO_3$. *Phys. Rev. B* **2005**, *71*, No. 024116.
(21) Horrocks, G. A.; Braham, E. J.; Liang, Y.; De Jesus, L. R.; Jude, J.; Velázquez, J. M.; Prendergast, D.; Banerjee, S. Vanadium K-Edge X-ray Absorption Spectroscopy as a Probe of the Heterogeneous Lithiation of V2O5: First-Principles Modeling and Principal Component Analysis. *J. Phys. Chem. C* **2016**, *120*, 23922−23932.
(22) Kim, B. Y.; Yun, J.-I. Optical Absorption and Fluorescence Properties of Trivalent Lanthanide Chlorides in High Temperature Molten LiCl-KCl Eutectic. *J. Lumin.* **2016**, *178*, 331−339.
(23) Yevick, A.; Frenkel, A. I. Effects of Surface Disorder on EXAFS Modeling of Metallic Clusters. *Phys. Rev. B* **2010**, *81*, No. 115451.
(24) Timoshenko, J.; Frenkel, A. I. Probing Structural Relaxation in Nanosized Catalysts by Combining EXAFS and Reverse Monte Carlo Methods. *Catal. Today* **2017**, *280*, 274−282.
(25) Chill, S. T.; Anderson, R. M.; Yancey, D. F.; Frenkel, A. I.; Crooks, R. M.; Henkelman, G. Probing the Limits of Conventional Extended X-ray Absorption Fine Structure Analysis Using Thiolated Gold Nanoparticles. *ACS Nano* **2015**, *9*, 4036−4042.
(26) Timoshenko, J.; Keller, K. R.; Frenkel, A. I. Determination of Bimetallic Architectures in Nanometer-Scale Catalysts by Combining Molecular Dynamics Simulations with X-ray Absorption Spectroscopy. *J. Chem. Phys.* **2017**, *146*, No. 114201.
(27) Price, S. W. T.; Zonias, N.; Skylaris, C.-K.; Hyde, T. I.; Ravel, B.; Russell, A. E. Fitting EXAFS Data Using Molecular Dynamics Outputs and a Histogram Approach. *Phys. Rev. B* **2012**, *85*, No. 075439.
(28) Ravel, B.; Newville, M. ATHENA, ARTEMIS, HEPHAESTUS: Data Analysis for X-ray Absorption Spectroscopy Using IFEFFIT. *J. Synchrotron Radiat.* **2005**, *12*, 537−541.
(29) Ferrari, A.; Braibanti, A.; Bigliardi, G. Refinement of the Crystal Structure of NiCl2 and of Unit-Cell Parameters of Some Anhydrous Chlorides of Divalent Metals. *Acta Crystallogr.* **1963**, *16*, 846−847.
(30) Frenkel, A. I.; Rehr, J. Thermal Expansion and x-ray-Absorption Fine-Structure Cumulants. *Phys. Rev. B* **1993**, *48*, 585−588.
(31) Frenkel, A. I.; Hills, C. W.; Nuzzo, R. G. A View from the Inside: Complexity in the Atomic Scale Ordering of Supported Metal Nanoparticles. *J. Phys. Chem. B* **2001**, *105*, 12689−12703.
(32) Farges, F.; Brown, G. E.; Rehr, J. Ti K-edge XANES Studies of Ti Coordination and Disorder in Oxide Compounds: Comparison Between Theory and Experiment. *Phys. Rev. B* **1997**, *56*, 1809−1819.
(33) Greenberg, J.; Sundheim, B. R. Absorption Spectra in Molten Salt Solutions. *J. Chem. Phys.* **1958**, *29*, 1029−1032.
(34) Gruen, D. M.; McBeth, R. L. The Coordination Chemistry of 3d Transition Metal Ions in Fused Salt Solutions. *Pure Appl. Chem.* **1963**, *6*, 23−48.
(35) Angell, C. A.; Wong, J. Structure and Glass Transition Thermodynamics of Liquid Zinc Chloride from Far-Infrared, Raman, and Probe Ion Electronic and Vibrational Spectra. *J. Chem. Phys.* **1970**, *53*, 2053−2066.

https://dx.doi.org/10.1021/acs.jpcb.0c00195
J. Phys. Chem. B 2020, 124, 1253−1258